Journal of Computational Physics **150,** 181–198 (1999)
Article ID jcph.1998.6170, available online at http://www.idealibrary.com on IDEAL®

Monotone Scheme and Boundary Conditions for Finite Volume Simulation of Magnetohydrodynamic Internal Flows at High Hartmann Number

L. Leboucher

Centre for Numerical Modelling and Process Analysis, University of Greenwich, London SE18 6PF, United Kingdom
E-mail: L.Leboucher@gre.ac.uk

Received August 3, 1998; revised November 23, 1998

A monotone scheme for finite volume simulation of magnetohydrodynamic internal flows at high Hartmann number is presented. The numerical stability is analysed with respect to the electromagnetic force. Standard central finite differences applied to finite volumes can only be numerically stable if the vector products involved in this force are computed with a scheme using a fully staggered grid. The electromagnetic quantities (electric currents and electric potential) must be shifted by half the grid size from the mechanical ones (velocity and pressure). An integral treatment of the boundary layers is used in conjunction with boundary conditions for electrically conducting walls. The simulations are performed with inhomogeneous electrical conductivities of the walls and reach high Hartmann numbers in three-dimensional simulations, even though a non-adaptive grid is used.

Key Words: magnetohydrodynamics; MHD; Hartmann layer; duct flow; numerical stability; finite volumes; finite differences; monotone scheme.

1. INTRODUCTION

Magnetohydrodynamic (MHD) duct flows have been extensively studied by asymptotic theory. However, very little work is based on inertial flows. Three-dimensional numerical simulations of inertial flows are often limited to the steady regime and are always limited to very low Hartmann numbers (Ha ~ 50) [1, 2]. The square of the Hartmann number is the ratio between the electromagnetic and the viscous forces. It is therefore a measure of the magnetic field strength for a given fluid in a duct of a given scale. Although some linear stability analysis is available [3], it is only recently that the non-linear regime has been investigated numerically with success at high Hartmann numbers (Ha ~ 1000) [14]. However, this recent work is strictly two-dimensional and concerns the flow between two infinite plates.

0021-9991/99 $30.00

In the present paper the full geometry of a duct is considered and the effect of the walls parallel to the magnetic field is shown. Moreover the simulations are performed in three dimensions, allowing the flow to depart from its two-dimensional structure.

Because the Hartmann layers are very thin, they are not treated numerically. The electric currents which close within the Hartmann layers are integrated analytically and added to the electric currents which close within the Hartmann walls. The numerical resolution is then only limited by the side layers parallel to the magnetic field. These layers are much thicker. While the thickness of the Hartmann layers scales with Ha^{-1}, that of the side layers scales with $\mathrm{Ha}^{-1/2}$. As a result the simulations are performed at a higher Hartmann number ($\mathrm{Ha} = 300$) than those of the former three-dimensional simulations, even though no adaptive grid is used.

1.1. *Governing Equations*

The flow of an electrically conducting fluid under the influence of an external magnetic field with negligible induced field is governed by the following equations [4] which express the conservation of mass and momentum,

$$\nabla \cdot \mathbf{u} = 0, \tag{1}$$

$$\frac{1}{N}\left(\frac{\partial \mathbf{u}}{\partial t} + (\mathbf{u}\cdot\nabla)\mathbf{u}\right) = -\nabla p + \mathbf{j}\times\hat{\mathbf{y}} + \frac{1}{\mathrm{Ha}^2}\nabla^2\mathbf{u}, \tag{2}$$

together with the conservation of electric charge and Ohm's laws,

$$\nabla \cdot \mathbf{j} = 0, \tag{3}$$

$$\mathbf{j} = -\nabla\Phi + \mathbf{u}\times\hat{\mathbf{y}}. \tag{4}$$

The duct has its axis in the x-direction and has a rectangular cross-section in the yz-plane. The magnetic field is uniform and aligned with the y-direction. The induced field is neglected. The dimensionless variables are scaled as follows. The three coordinates are expressed in terms of the length scale, a, chosen as the half width of the duct in the y-direction. The scale of the velocity $\mathbf{u}$ is the mean velocity v_0. The unit of time is the length scale divided by the mean velocity. The current density $\mathbf{j}$ is scaled with the product of the electrical conductivity σ of the fluid, the mean velocity, and the strength of the magnetic field $\mathbf{B}$. The magnetic field is scaled with its own strength B so that its dimensionless representation is the unit vector $\hat{\mathbf{y}}$.

As in the classical literature on the inertialess core flow solution, the pressure is scaled with the mass density ρ of the fluid times the square of the mean velocity times the interaction parameter $N = \sigma B^2 a/(\rho v_0)$. In this way, a stationary fully developed flow in a straight duct is governed in its core by the balance between the pressure gradient and the Lorentz force, the viscous terms being negligible outside the region of strong shear. The present work, however, keeps all terms.

There are two dimensionless parameters in this problem. The interaction parameter N characterises the ratio between the electromagnetic and the inertia forces, and the Hartmann number squared is defined as $\mathrm{Ha}^2 = \sigma B^2 a^2/\mu$, where μ is the dynamic viscosity of the fluid. The Reynolds number may be expressed as the ratio between these two parameters:

$$\mathrm{Re} = \frac{\mathrm{Ha}^2}{N}. \tag{5}$$

2. NUMERICAL METHOD

2.1. *Conservative Form*

As usual in low-order finite differencing, it is preferable for accuracy and numerical stability to solve the equations in conservative form. Equation (2) may be written with the unit tensor $\overline{\overline{I}}$,

$$\frac{\partial \mathbf{u}}{\partial t} + \nabla \cdot (\mathbf{u} \otimes \mathbf{u} + Np\overline{\overline{I}} - \mathrm{Re}^{-1}\nabla \mathbf{u}) = N\mathbf{j} \times \hat{\mathbf{y}}. \tag{6}$$

2.2. *Time Discretisation and Integration Method*

The electric current density $\mathbf{j}^n$ at the time step n is computed from Ohm's law. The electric potential is computed as the solution of the Poisson equation (8) obtained from the divergence of Ohm's law (7), assuming conservation of charge $\nabla \cdot \mathbf{j}^n = 0$:

$$\mathbf{j}^n = -\nabla \Phi^n + \mathbf{u}^n \times \hat{\mathbf{y}}, \tag{7}$$

$$\nabla^2 \Phi^n = \nabla \cdot (\mathbf{u}^n \times \hat{\mathbf{y}}). \tag{8}$$

All other terms are evaluated explicitly, with the exception of the pressure. The time dependence of the solution is treated with the so-called "fractional step" method [7, 8]. It can be summarised by the following three equations.

First, consider the time-discretised Navier–Stokes equations in conservative form,

$$\frac{\mathbf{u}^{n+1} - \mathbf{u}^n}{\Delta t} + \nabla \cdot (\mathbf{u}^n \otimes \mathbf{u}^n + Np\overline{\overline{I}} - \mathrm{Re}^{-1}\nabla \mathbf{u}^n) = N\mathbf{j}^n \times \hat{\mathbf{y}}. \tag{9}$$

Second, take the divergence of this equation in order to obtain the following Poisson-type equation which can be solved for pressure since its right-hand side is known explicitly at the previous time step n:

$$\nabla^2 p = \nabla \cdot \mathbf{A}^n \qquad \text{where } \mathbf{A}^n = -\frac{1}{N}\nabla \cdot (\mathbf{u}^n \otimes \mathbf{u}^n) + \mathbf{j}^n \times \hat{\mathbf{y}} + \frac{1}{\mathrm{Ha}^2}\nabla^2 \mathbf{u}^n. \tag{10}$$

Third, the velocity at the next time step $n+1$ is evaluated with a first-order scheme as

$$\mathbf{u}^{n+1} = \mathbf{u}^n + N\Delta t \mathbf{A}^n - N\Delta t \nabla p \tag{11}$$

or with a second-order Adams–Bashforth scheme, which is preferred for unsteady flows, in which case

$$\nabla^2 p = \nabla \cdot \left(\frac{3}{2}\mathbf{A}^n - \frac{1}{2}\mathbf{A}^{n-1}\right), \tag{12}$$

$$\mathbf{u}^{n+1} = \mathbf{u}^n + \frac{3}{2}N\Delta t \mathbf{A}^n - \frac{1}{2}N\Delta t \mathbf{A}^{n-1} - N\Delta t \nabla p. \tag{13}$$

2.3. *Spatial Discretisation for Velocity and Pressure*

The code is based on a three-dimensional finite volume discretisation, on an orthogonal equally spaced grid. The code was initially written with a classical structured finite volume mesh with all vector quantities at the surfaces of each cell and all scalar quantities in the

middle of the cell (Fig. 4). All derivatives are discretised as central second-order finite differences such as

$$\left.\frac{\partial p}{\partial x}\right|_{i+1/2,\,j,k} = \frac{p_{i+1,j,k} - p_{i,j,k}}{\Delta x}. \tag{14}$$

As the advective term is written in divergence form, its x-component is computed as

$$\nabla \cdot (u\mathbf{u}) = \frac{\partial u^2}{\partial x} + \frac{\partial (uv)}{\partial y} + \frac{\partial (uw)}{\partial z} \tag{15}$$

with

$$\left.\frac{\partial u^2}{\partial x}\right|_{i+1/2,\,j,k} = \frac{u^2_{i+1,j,k} - u^2_{i,j,k}}{\Delta x} \tag{16}$$

and

$$\left.\frac{\partial (uv)}{\partial y}\right|_{i+1/2,\,j,k} = \frac{u_{i+1/2,\,j+1/2,k} v_{i+1/2,\,j+1/2,k} - u_{i+1/2,\,j-1/2,k} v_{i+1/2,\,j-1/2,k}}{\Delta y}, \tag{17}$$

where

$$\begin{aligned} u_{i,j,k} &= \frac{1}{2}(u_{i+1/2,\,j,k} + u_{i-1/2,\,j,k}), \\ u_{i+1/2,\,j+1/2,k} &= \frac{1}{2}(u_{i+1/2,\,j+1,k} + u_{i+1/2,\,j,k}), \\ v_{i+1/2,\,j+1/2,k} &= \frac{1}{2}(v_{i+1,\,j+1/2,k} + v_{i,\,j+1/2,k}), \end{aligned}$$

and similar definitions apply to $u_{i+1,\,j,k}$, $u_{i+1/2,\,j-1/2,k}$, $v_{i+1/2,\,j-1/2,k}$ and $\partial(uw)/\partial z$.

The Laplacians of p and Φ, and similarly the Laplacians of the three velocity components, are discretised with ordinary second-order central differences:

$$\begin{aligned} \nabla^2 p|_{i,j,k} = &\frac{p_{i+1,j,k} - 2p_{i,j,k} + p_{i-1,j,k}}{\Delta x^2} + \frac{p_{i,j+1,k} - 2p_{i,j,k} + p_{i,j-1,k}}{\Delta y^2} \\ &+ \frac{p_{i,j,k+1} - 2p_{i,j,k} + p_{i,j,k-1}}{\Delta z^2}. \end{aligned}$$

3. NUMERICAL STABILITY WITH RESPECT TO THE ELECTROMAGNETIC TERMS

As the current density $\mathbf{j}$ as defined in Eq. (4) is the sum of two terms, the Lorentz force is the sum of the two terms at the right of the equation

$$\mathbf{j} \times \hat{\mathbf{y}} = -\nabla\Phi \times \hat{\mathbf{y}} + (\mathbf{u} \times \hat{\mathbf{y}}) \times \hat{\mathbf{y}}. \tag{18}$$

If one first computes $\mathbf{u} \times \hat{\mathbf{y}}$ and then $(\mathbf{u} \times \hat{\mathbf{y}}) \times \hat{\mathbf{y}}$ using a standard staggered grid, the resulting finite difference scheme is unstable for either high Hartmann number (strong magnetic field) or coarse grid spacing in the direction perpendicular to both the magnetic field and to the velocity (z-direction). This numerical instability is characterised by strong local oscillations and unphysical jets at the corners of the duct as shown in Fig. 2. The reason for this instability lies in the finite difference scheme resulting from the staggered grid itself. Indeed, $\mathbf{u} \times \hat{\mathbf{y}}$ is

perpendicular to $\mathbf{u}$ and cannot occupy the same staggered grid points as $\mathbf{u}$ (Fig. 1). Once $\mathbf{u} \times \hat{\mathbf{y}}$ is computed, the same problem occurs when computing $(\mathbf{u} \times \hat{\mathbf{y}}) \times \hat{\mathbf{y}}$. Finally, the Lorentz force computed as Eq. (18) can only result in an averaging of different values of $\mathbf{u}$ at several grid points, and it can be shown that this scheme is not monotone unless the grid spacing in the z-direction is scaled proportionally to the inverse of the Hartmann number. This result can be guessed by writing the full discretised equation of the explicit scheme, in terms of the contribution of each grid point to the value of the velocity at the new time step. The analysis of the monotonicity of the scheme will then help in finding the origin of the numerical instability.

Such a development, however, needs some assumption. The classical literature on numerical simulation deals with the numerical stability of finite differences schemes for convection–diffusion equations without a pressure term. The criteria obtained for numerical stability are commonly used for the numerical solution of the Navier–Stokes equations, even though they do not take the pressure term into account. Indeed, including the pressure in the numerical stability analysis is not trivial, as it has no explicit expression and depends on the boundary conditions. Nevertheless the classical Courant–Friedrich–Lewy (CFL) criterion and the time step limitation in terms of the diffusion time scaled on the mesh interval are commonly and successfully applied to the Navier–Stokes equations, although they are derived for pure convection–diffusion equations.

In the following stability analysis, the pressure gradient will be dropped as well as the electric potential. Indeed, the electric potential is computed similarly to the pressure. There is no explicit expression for this scalar which is the solution of a Poisson equation depending on the boundary conditions, just like the pressure. It will later be shown, from the numerical experiments, that the conditions obtained from this analysis apply successfully to the original set of MHD equations (1)–(4) discretised as (6)–(11). After dropping the electric potential, only the term $(\mathbf{u} \times \hat{\mathbf{y}}) \times \hat{\mathbf{y}}$ remains in the expression of the Lorentz force.

As usual in numerical stability analysis, the advection term is linearised so that $\nabla \cdot (\mathbf{u} \otimes \mathbf{u})$ is replaced with $\nabla \cdot (\mathbf{u}_0 \otimes \mathbf{u})$, where $\mathbf{u}_0$ is supposed to be constant. The momentum equation (6) is then reduced to

$$\frac{\partial \mathbf{u}}{\partial t} + \nabla \cdot \left(\mathbf{u}_0 \otimes \mathbf{u} - \mathrm{Re}^{-1} \nabla \mathbf{u}\right) = N \mathbf{j} \times \hat{\mathbf{y}} = N (\mathbf{u} \times \hat{\mathbf{y}}) \times \hat{\mathbf{y}}. \tag{19}$$

3.1. *Numerical Instability Due to the Electromagnetic Term*

Let us write the finite difference scheme for the electromagnetic term. As $\mathbf{u} \times \hat{\mathbf{y}}$ is perpendicular to $\mathbf{u}$, it cannot be discretised on the same edge a finite volume as the edge where $\mathbf{u}$ lies. Therefore, $\mathbf{u} \times \hat{\mathbf{y}}$ has to be averaged from four neighbouring points, as pictured in Fig. 1. Then, the same problem occurs for $(\mathbf{u} \times \hat{\mathbf{y}}) \times \hat{\mathbf{y}}$. In the end, the Lorentz force is averaged from the values of $\mathbf{u}$ at nine different grid points. For instance, its x-component is

$$\begin{aligned}(\mathbf{u} \times \hat{\mathbf{y}}) \times \hat{\mathbf{y}}|_{x_{i+1/2,j,k}} = &-\frac{1}{4} u_{i+1/2,j,k} - \frac{1}{8} u_{i+3/2,j,k} - \frac{1}{8} u_{i-1/2,j,k} - \frac{1}{8} u_{i+1/2,j,k+1} \\ &- \frac{1}{8} u_{i+1/2,j,k-1} - \frac{1}{16} u_{i+3/2,j,k+1} - \frac{1}{16} u_{i+3/2,j,k-1} \\ &- \frac{1}{16} u_{i-1/2,j,k+1} - \frac{1}{16} u_{i-1/2,j,k-1}.\end{aligned} \tag{20}$$

For simplicity, suppose that the velocity $\mathbf{u} = (u, v, w)$ is such that $v = w = 0$, which corresponds to a fully developed laminar flow in a straight duct. Then the finite difference

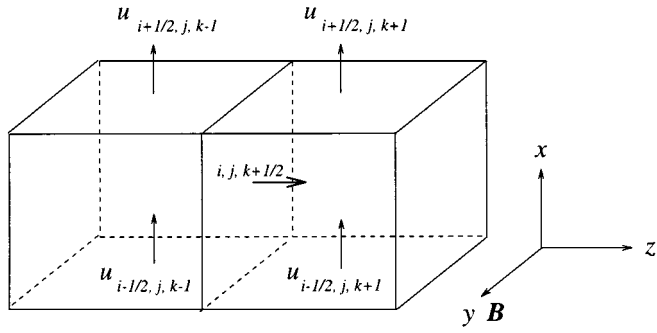

FIG. 1. Construction of a vector product from four points on a staggered grid: z-component of the $\mathbf{u} \times \hat{\mathbf{y}}$ in the electromagnetic force.

scheme for the MHD convection–diffusion equation (19) discretised in time with a first-order approximation similar to (11) reduces to the explicit form

$$\begin{aligned} u^{n+1}_{i+1/2,j,k} = {} & a_1 u^n_{i+1/2,j,k} + a_2 u^n_{i+3/2,j,k} + a_3 u^n_{i-1/2,j,k} + a_4 u^n_{j+1/2,j+1,k} + a_5 u^n_{i+1/2,j-1,k} \\ & + a_6 u^n_{i+1/2,j,k+1} + a_7 u^n_{i+1/2,j,k-1} + a_8 u^n_{i+3/2,j,k+1} + a_9\, u^n_{i+3/2,j,k-1} \\ & + a_{10} u^n_{i-1/2,j,k+1} + a_{11} u^n_{i-1/2,j,k-1}, \end{aligned} \tag{21}$$

with

$$\begin{aligned} a_1 &= 1 - \frac{1}{4}\Delta t N - 2\Delta t(\Delta x^{-2} + \Delta y^{-2} + \Delta z^{-2})\mathrm{Re}^{-1} \\ a_2 &= -\frac{1}{2}\Delta t \Delta x^{-1} u_0 - \frac{1}{8}\Delta t N + \Delta t \Delta x^{-2}\,\mathrm{Re}^{-1} \\ a_3 &= +\frac{1}{2}\Delta t \Delta x^{-1} u_0 - \frac{1}{8}\Delta t N + \Delta t \Delta x^{-2}\,\mathrm{Re}^{-1} \\ a_4 &= a_5 = \Delta t \Delta y^{-2}\,\mathrm{Re}^{-1} \\ a_6 &= a_7 = -\frac{1}{8}\Delta t N + \Delta t \Delta z^{-2}\,\mathrm{Re}^{-1} \\ a_8 &= a_9 = a_{10} = a_{11} = -\frac{1}{16}\Delta t N. \end{aligned}$$

This scheme is not monotone [10], as the coefficients $a_8, \ldots, a_{11}$ are always negative. The coefficients a_1, a_2, a_3 and a_6, a_7 are also negative when the following conditions are not satisfied:

$$\Delta t \le \frac{\mathrm{Re}}{2(\Delta x^{-2} + \Delta y^{-2} + \Delta z^{-2}) + \frac{1}{4}\mathrm{Re}\, N} \tag{22}$$

$$\mathrm{Re}|u_0|\Delta x \le \frac{2}{1 + \frac{N}{4}\frac{\Delta x}{|u_0|}} \tag{23}$$

$$\Delta z \le \frac{2\sqrt{2}}{\mathrm{Ha}}. \tag{24}$$

However, monotonicity is a strong condition for numerical stability. While a monotone scheme is numerically stable, a non-monotone scheme may be stable. The numerical experiments show that the conditions (22)–(23) actually hold for stability. When these conditions

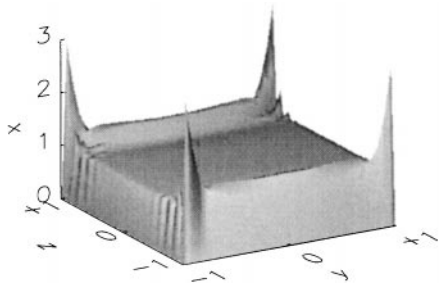

FIG. 2. Velocity $u = f(y, z)$ at $\mathrm{Ha} = 200$ with unstable scheme.

are satisfied, the scheme is stable, even though the coefficients $a_8, \ldots, a_{11}$, corresponding to the furthest location $i + \frac{1}{2} \pm 1$, $j, k \pm 1$ from the central grid point $i + \frac{1}{2}$, j, k, are negative. When these conditions are not satisfied, the scheme is unstable. Equation (22) is the diffusion limitation on the time step. Compared to classical computational fluid dynamics, this limitation is stronger, as it includes an electromagnetic term at the denominator. Equation (23) is a mesh Reynolds number limitation and can be rewritten as a limitation on Δx:

$$\Delta x \leq -\frac{2u_0}{N} + \sqrt{\left(\frac{2u_0}{N}\right)^2 + \frac{8}{\mathrm{Ha}^2}} \leq \frac{2\sqrt{2}}{\mathrm{Ha}}. \tag{25}$$

Most important is the condition (24), which has no equivalent to classical CFD. The numerical simulations of the three-dimensional code show numerical instabilities, as seen in Fig. 2, when this condition is not satisfied and the walls of the channel are electrically conducting. When the walls are electrically insulating, this condition does not hold; the simulations remain numerically stable provided the other conditions (22) and (23) are satisfied. Unfortunately, applications of MHD duct flows such as lithium blankets for fusion reactors imply that the walls are made of steel, and any coating of the interior of the duct with some insulating material is made difficult by the conditions of use under high temperature. The strongest numerical oscillations appear with a perfectly conducting wall. They decrease with lower conductivities, but are present as soon as the walls are not insulating. This is consistent with the previous simulations [1] and [2], where all simulations at relatively large Ha numbers are performed with insulating walls while the simulations with conducting walls are limited to $\mathrm{Ha} = 50$ on a grid of 32×32 points in the cross section of the duct, i.e., with $\Delta y = \Delta z = 1/16$. The condition (24) for such a Hartmann number is $\Delta z < 1/17.7$.

This problem is the strongest limitation of the scheme (21). The length Δz which corresponds to the space discretisation in the direction perpendicular to the side layers should be inversely proportional to the Hartmann number. This implies that these layers should be discretised as if they were as thin as the Hartmann layers; while the numerical resolution of the side layers only implies that $\Delta z \propto \mathrm{Ha}^{-1/2}$, the numerical stability implies that $\Delta z \propto \mathrm{Ha}^{-1}$, leading to unnecessarily fine meshes at high Ha.

3.2. *Stable Scheme for the Electromagnetic Terms*

An alternative is to compute the Lorentz force from the following equation which involves the component $\mathbf{u}_\perp = -(\mathbf{u} \times \hat{\mathbf{y}}) \times \hat{\mathbf{y}}$ of the velocity, perpendicular to the magnetic

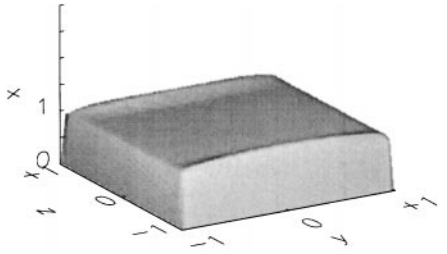

FIG. 3. Velocity $u = f(y, z)$ at Ha = 200 with stable scheme.

field (Fig. 3):

$$\mathbf{j} \times \hat{\mathbf{y}} = -\nabla\Phi \times \hat{\mathbf{y}} - \mathbf{u}_\perp. \tag{26}$$

The x-component of the double vector product is then simply

$$(\mathbf{u} \times \hat{\mathbf{y}}) \times \hat{\mathbf{y}}|_{x_{i+1/2,j,k}} = -u_{i+1/2,j,k}. \tag{27}$$

Thus, the finite difference scheme for the MHD convection–diffusion equation (19) reduces to

$$\begin{aligned} u^{n+1}_{i+1/2,j,k} = {} & a'_1 u^n_{i+1/2,j,k} + a'_2 u^n_{i+3/2,j,k} + a'_3 u^n_{i-1/2,j,k} + a'_4 u^n_{j+1/2,j+1,k} + a'_5 u^n_{i+1/2,j-1,k} \\ & + a'_6 u^n_{i+1/2,j,k+1} + a'_7 u^n_{i+1/2,j,k-1}, \end{aligned} \tag{28}$$

with

$$\begin{aligned} a'_1 &= 1 - \frac{1}{4}\Delta t N - 2\Delta t(\Delta x^{-2} + \Delta y^{-2} + \Delta z^{-2})\mathrm{Re}^{-1} \\ a'_2 &= -\frac{1}{2}\Delta t \Delta x^{-1} u_0 + \Delta t \Delta x^{-2}\,\mathrm{Re}^{-1} \\ a_3 &= \frac{1}{2}\Delta t \Delta x^{-1} u_0 + \Delta t \Delta x^{-2}\,\mathrm{Re}^{-1} \\ a'_4 &= a'_5 = \Delta t \Delta y^{-2}\,\mathrm{Re}^{-1} \qquad \text{and} \qquad a'_6 = a'_7 = \Delta t \Delta z^{-2}\,\mathrm{Re}^{-1}. \end{aligned}$$

This scheme is monotone as long as the following conditions are satisfied:

$$\Delta t \le \frac{\mathrm{Re}}{2(\Delta x^{-2} + \Delta y^{-2} + \Delta z^{-2}) + \mathrm{Re}\, N} \tag{29}$$

$$\mathrm{Re}|u_0|\Delta x \le \frac{2}{1 + \frac{N}{4}\frac{\Delta x}{|u_0|}}. \tag{30}$$

Its stability is *independent* of how coarse the grid is in the direction perpendicular to both velocity and magnetic field.

3.3. *Accurate Scheme for the Electromagnetic Terms and Fully Staggered Grid*

Unfortunately, the numerically stable scheme for $(\mathbf{u} \times \hat{\mathbf{y}}) \times \hat{\mathbf{y}}$ as defined above is inaccurate when it is used together with the $-\nabla\Phi \times \hat{\mathbf{y}}$ term of the Lorentz force (18) discretised

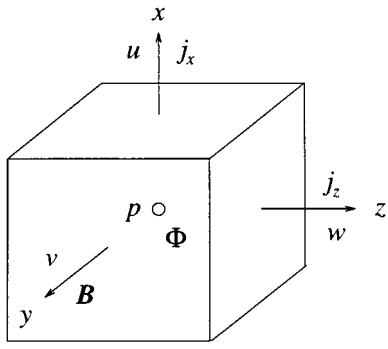

FIG. 4. Ordinary staggered grid.

on an ordinary staggered grid (Fig. 4). Indeed, the derivative $\partial\Phi/\partial z$ involved in the term $-\nabla\Phi\times\hat{\mathbf{y}}$, which needs to be known at the grid point $i+\frac{1}{2}, j, k$ before it is added to the x-component of the momentum Eq. (19), can only be written as an average of finite differences centred at i, j, k and $i+1, j, k$,

$$\left.\frac{\partial\Phi}{\partial z}\right|_{i+1/2,j,k}=\frac{1}{2}\left(\frac{\Phi_{i,j,k+1}-\Phi_{i,j,k-1}}{2\Delta z}+\frac{\Phi_{i+1,j,k+1}-\Phi_{i+1,j,k-1}}{2\Delta z}\right), \tag{31}$$

unless a higher order interpolation involving more grid points is used.

A better scheme for $\partial\Phi/\partial z$ is obtained if a fully staggered grid (Fig. 5) is used, as already pointed out by the author [12]. Such a grid was first used in a large eddy simulation of MHD duct flow by Shimomura [11] at $\mathrm{Ha}=50$. On this grid, the derivative of Φ can then be discretised more simply as

$$\left.\frac{\partial\Phi}{\partial z}\right|_{i+1/2,j,k}=\frac{\Phi_{i+1/2,j,k+1/2}-\Phi_{i+1/2,j,k-1/2}}{\Delta z}. \tag{32}$$

This form (32) is also more accurate than (31). Moreover, if the accurate scheme (27) for $(\mathbf{u}\times\hat{\mathbf{y}})\times\hat{\mathbf{y}}=-\mathbf{u}_\perp$ is combined with the less accurate scheme (31) in $-\nabla\Phi\times\hat{\mathbf{y}}$, then the results are not only inaccurate but completely wrong. Numerical tests on fully developed flows show that the velocity profile $u(y,z)$ at a given Ha number looks like that of a flow at a much lower Ha number; the side layers are much thicker than they should be. Although

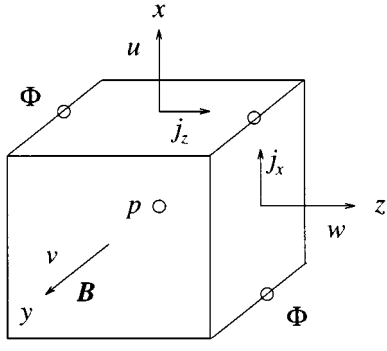

FIG. 5. Fully staggered grid.

the scheme is consistent, its convergence with respect to the refinement of the grid cannot be afforded with reasonable computer power at Hartmann numbers as moderate as 100 and becomes impossible at higher values of this number.

The reason for this poor convergence can be seen easily. Let us neglect the variations of u along the magnetic field $\hat{y}$, which are much smaller in the side layers compared to those in the z-direction. Then the error of the scheme (31) in $-\nabla\Phi \times \hat{\mathbf{y}}$ is at leading order $(\Delta z^2/6)(\partial^3\Phi/\partial z^3)$ while that of the scheme (32) is only $(\Delta z^2/24)(\partial^3\Phi/\partial z^3)$. However, the inaccurate scheme (31) used with the averaged scheme (20) for $(\mathbf{u} \times \hat{\mathbf{y}}) \times \hat{\mathbf{y}}$ gives, when it is stable, the same results as those of the accurate scheme (32) combined with the exact value (27). The reason for this is that the schemes (20) and (31) accumulate two errors which almost cancel each other. Indeed, the finite difference (20) gives a negative error of order $-(\Delta z^2/4)(\partial^2 u/\partial z^2)$.

In the end, it turns out that the numerically stable scheme (32) has to be used with a fully staggered grid so that (26)–(27) is used for an accurate computation of the Lorentz force. Therefore, this combination is retained for the simulations described here.

The numerical experiments with the three-dimensional time-dependent scheme (6)–(11) corresponding to the set of MHD equations (1)–(4) show that the scheme is numerically stable under the monotonicity conditions (29) and (30), although these conditions were guessed from simpler equations. When these conditions are not satisfied, the simulations are found to be numerically unstable. In the case where the diffusion–time limitation (29) is not satisfied, strong oscillations give an overflow after a few time steps. When only the mesh Reynolds number condition (30) is not satisfied, small oscillations appear and amplify slowly. They can be avoided if an upwind scheme is used. A second-order upwind scheme [9] is actually used here when the mesh Reynolds number is greater than two. Then the influence of the Lorentz force on numerical stability remains only in the condition (29). The diffusion limitation on the time step is stronger than that of the scheme (21) of the ordinary staggered grid.

Finally, the fully staggered grid, together with the schemes (27) and (32), is the best choice for explicit finite volume computation of MHD flow with standard second-order central finite differences. Indeed, the most restrictive stability condition on the Hartmann number (24) is avoided and the mesh Reynolds number limitation is not altered by the electromagnetic force. Figure 3 gives an example of velocity profile obtained with these schemes using the same parameters ($\mathrm{Ha} = 200$) as for the numerically unstable example (Fig. 2). Another example at even higher Hartmann number ($\mathrm{Ha} = 1000$) and with the special treatment of the Hartmann layers described in the next section is given in Fig. 8. Runs of unsteady flows will be found in the last section.

4. BOUNDARY CONDITIONS

4.1. *Arbitrary Conductivity of the Walls*

The walls can have an arbitrary electrical conductivity σ_w, and the currents in these boundaries are calculated using the thin wall condition. The thickness ϵ of the walls is supposed to be much smaller than the half-width of the duct ($\epsilon \ll a$) so that the currents in the walls are modelled as a sheet of current.

The normal component of the current coming from the fluid is a source for the current in the wall. Therefore it gives rise to a nonzero divergence of the two-dimensional current

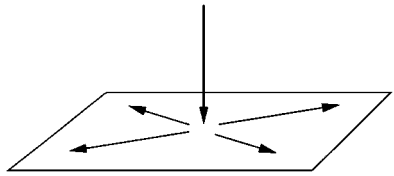

FIG. 6. Electric current coming from the fluid and diverging onto an electrically conducting wall.

in the wall (Fig. 6). The relation between the currents can be written as Eq. (33), in terms of the electric potential and the wall conductance ratio c, by splitting the gradient operator into its components normal and tangential to the wall:

$$\nabla_n \Phi = \nabla_t \cdot (c \nabla_t \Phi) \qquad \text{with } c = \frac{\sigma_w \epsilon}{\sigma a}. \tag{33}$$

The boundary conditions on the electric potential in the three-dimensional Poisson equation (8) should match the conservation law (33) for the currents in the walls. For this reason, the code uses an iterative procedure, which differs from a previous work in the sense that it does not call a two-dimensional Poisson solver to find the potential on the walls.

One starts with Neumann boundary conditions by setting its value at the previous iteration. Then, the Poisson equation in the fluid (8) is solved. Now, the potential has a value everywhere, including the walls, and the right-hand side of Eq. (33) can be calculated. The Poisson equation (8) is solved again with new Neumann boundary conditions, now defined as Eq. (33). The iteration is performed until convergence is reached. The convergence is faster when using the relaxation parameter $\omega < 1$, such that

$$\nabla_n \Phi^{\text{new}} = (1 - \omega) \nabla_n \Phi^{\text{old}} + \omega \nabla_n \Phi^{\text{older}}. \tag{34}$$

When starting the program, the first time step may need 100 or more iterations, while the following time steps need only an adjustment with respect to the previous time step and therefore only need a few iterations. A maximum of approximately 10 iterations are needed for the most unstable cases described in the last section.

4.2. *Integral Treatment of the Hartmann Layer*

The Hartmann layers, which are the layers perpendicular to the magnetic field, have a thickness $\delta = \text{Ha}^{-1}$ inversely proportional to the Hartmann number. For very high values of Ha, they are so thin that it is hard to resolve them numerically. Therefore, Hartmann layers are treated here analytically, using the integral relation that links properties of the core with the variables at the wall and which have been used for inertialess MHD channel flow simulations [5]. The solution in the core as well as in the side layers is obtained according to the three-dimensional numerical scheme presented in the previous paragraphs. The task is therefore to use conditions which apply to the core variables instead of the physical boundary conditions for the fluid at the Hartmann wall.

In the Hartmann layers the currents find a path to close their circuit as they do within conducting walls. The Hartmann layers act like an additional conducting sheet parallel to the conducting walls. The conductivity used in the thin wall condition defined by Eq. (33) is therefore effectively increased by the integral conductivity of the Hartmann layers, which

is proportional to their thickness:

$$\nabla_n \Phi = \nabla_t \cdot [(c + \delta)\nabla_t \Phi]. \tag{35}$$

The potential does not vary across the Hartmann layer to the leading order of approximation so that the current component normal to the wall is still well represented by the normal component of the core potential gradient.

Once the core solution is known, the solution within the layers can be reconstructed if desired. It is known that the velocity components tangential to the wall decay exponentially towards the wall.

$$\mathbf{u}_t = \mathbf{u}_t^C (1 - e^{-\mathrm{Ha}\, n}). \tag{36}$$

Note that n stands here for the coordinate along the inward normal to the wall and the superscript C denotes values of the core velocities. The component normal to the wall of the core velocity is obtained by integrating the equation for the conservation of mass, $\nabla \cdot \mathbf{u} = 0$, across the layer. This leads to the condition

$$\mathbf{u}_n^C = \mathrm{Ha}^{-1}\, \nabla_t \cdot \mathbf{u}_t^C. \tag{37}$$

In the code, the high Hartmann number limit is implemented,

$$\mathbf{u}_n^C = 0 \qquad \text{as } \mathrm{Ha} \to \infty. \tag{38}$$

The kinematic conditions for the tangential components of the core velocity are estimated at the wall by a linear or second-order extrapolation of the core solution. Higher order extrapolations were also used and did not significantly change the results.

Figure 7 shows the velocity profile of a fully developed flow at $\mathrm{Ha} = 50$ with a finite conductivity of the walls ($c = 0.05$) and a resolution of $n_y \times n_z = 32 \times 32$ grid points in the cross section. In Fig. 8, the most difficult parameters were chosen while keeping the same total number of grid points as the resolution is set to $n_y \times n_z = 8 \times 128$. The Hartmann number is as high as $\mathrm{Ha} = 1000$. This number could not be reached without the analytical treatment of the Hartmann layers. The walls are perfectly conducting. While this is the worst case in terms of numerical stability, as mentioned in Section 3, the code remains numerically stable. Compared to Hunt's exact analytical solution [6] in the case of conducting Hartmann walls and insulating side walls corresponding to high velocity jets, the accuracy of the code at $\mathrm{Ha} = 100$ is 7% for a resolution of $n_y \times n_z = 8 \times 32$, 2% for $n_y \times n_z = 16 \times 64$, and 0.3% for $n_y \times n_z = 32 \times 128$.

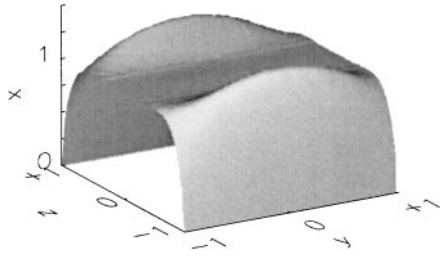

FIG. 7. Analytical treatment of the thin Hartmann layers. Fully developed velocity profile $u = f(y, z)$ at $\mathrm{Ha} = 50$ with the wall conductance ratio $c = 0.05$ and a resolution of 32×32. The velocity in the thin Hartmann layers is not displayed.

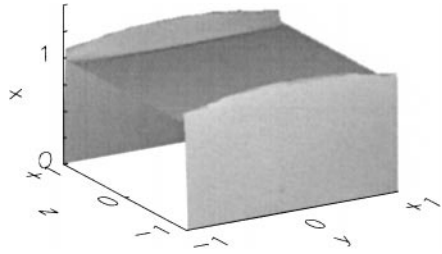

FIG. 8. Same as Fig. 7 but at the very high Hartmann number Ha = 1000 and with perfectly conducting walls. The resolution is 8×128 (same total number of grid points). The extremely thin Hartmann layers are not displayed.

5. SIMULATIONS

5.1. *Introduction*

Magnetic fields tend to damp instabilities in electrically conducting fluids. This effect is unwanted for some applications where high heat transfer and turbulence are preferred. In order to enhance the instability of a flow through an insulating duct, the walls perpendicular to the magnetic field can be supplied with a pair of electrically conducting strips (Fig. 9), as was originally proposed by Kolesnikov [13]. This device was used by this author to study MHD shear layers. It may also be used as a turbulence promoter in order to improve the cooling of fusion reactors. Recently, it has been modelled analytically and numerically by Bühler [14] as a two-dimensional flow between two infinite plates and investigated experimentally by Debray [15].

5.2. *Flow between Two Infinite Plates with a Conducting Strip*

First, the code was tested with respect to the results obtained in two dimensions by Bühler. The code was run with no stress boundary conditions at the side walls, using the following parameters: Ha = 1000; ratio of the distance between the two plates to the strip width = 10; insulating Hartmann walls; size of the grid in x, y, z-directions = $27 \times 16 \times 128$ cells; computational domain: $0 < x < \lambda$, where $\lambda = 0.802$, $-1 < y < +1$, $-1 < z < +1$; conductivity of the strip $c_0 = 4.2 \times 10^2$; ratio of the width of the channel to the width of the strip $a_r = 10$, the conductivity of the strip being smoothed at the edges as in Ref. [14],

$$c = \frac{c_0}{1 + \left(\frac{\sinh z}{\sinh a_r^{-1}}\right)^6}. \tag{39}$$

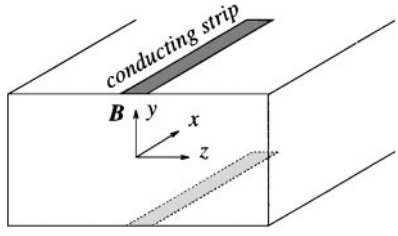

FIG. 9. Duct with electrically conducting strips.

The code is run with periodic boundaries at the inlet and outlet, separated by a distance equal to the wavelength λ of the instability, which is given by the linear stability analysis.

The critical Reynolds number for the onset of the instability is between 2000 and 2100 for the three-dimensional code, and 1800 for the two-dimensional code and the linear stability analysis. The Reynolds number is based on the velocity far from the strip. The same pattern is found on the vorticity lines on both codes for a higher Reynolds number of 4000. The discrepancy in the critical Reynolds number may have its origin in the higher numerical diffusion of the three-dimensional code compared to the two-dimensional code, which uses a higher resolution in the plane perpendicular to the magnetic field.

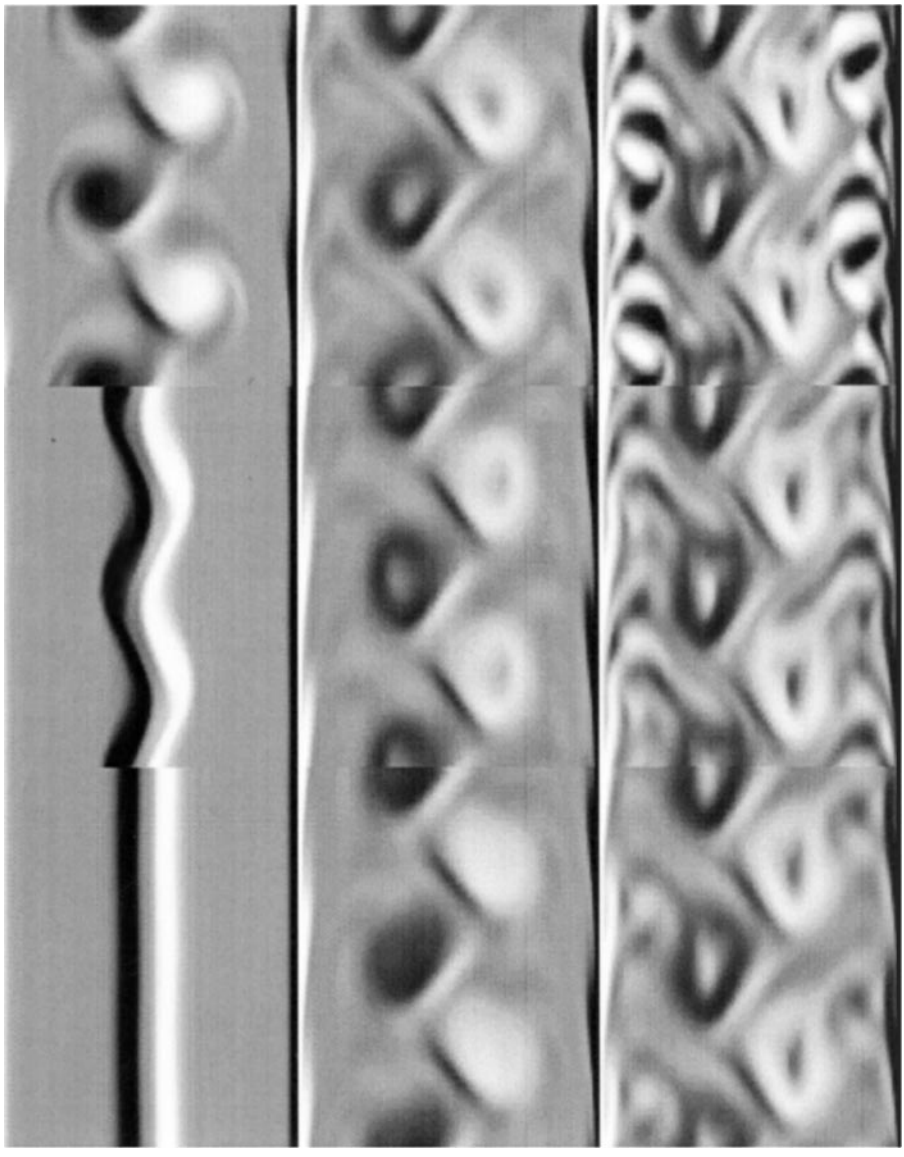

FIG. 10. Evolution of a magnetohydrodynamic shear layer created by electrically conducting strips in a duct (see geometry in Fig. 9). View of the y-component of the vorticity in the plane ($y = 0$). The frames are ordered from bottom to top and from left to right at the dimensionless time intervals 2.5, 5.0, 7.0, 10, 12.5, 15.0, 17.5, 20, and 22.5 from the initial perturbation.

5.3. *Unstable Flow in a Duct with Conducting Strips*

The code is run for the same parameters as the experiment performed by Debray [15]. The parameters of the experiment and its numerical simulation are the following: Ha = 300; $N = 29$; Re = 3108; ratio of the distance between the two plates to the strip width $a_r = 6$; all walls insulating; size of the grid in x, y, z-directions $= 27 \times 16 \times 128$ cells; computational domain: $0 < x < (\lambda = 2.79)$ and $-2 < y < +2$, $-1 < z < +1$; conductivity of the strip $c_0 = 4.2 \times 10^{-2}$; and half width of the strips $a_r = 0.167$. The Reynolds number is now based on the mean velocity that can be deduced from the flow rate. The flow rate is kept constant throughout the simulation. The length of the computational domain is set to the wavelength that was found experimentally. Note that the figures represent the solution for two wave-lengths, although the computational domain extends over one wavelength only.

The simulation is initialised with a small perturbation on the velocity. This perturbation is rapidly amplified as large eddies around the strip (Fig. 10). The flow is essentially two dimensional, as shown by the y-component of vorticity plotted at different y-levels of the duct (Fig. 11). The component v of the velocity parallel to the magnetic field differs from zero only in the region of strong shear (Fig. 11). It remains very small, about 50 times smaller than the maximum value of w.

During a transient period, these vortices grow relatively slowly compared to the initial small perturbation and develop from the strip to the side walls. When they reach the side layers, some new vortices are created and develop from the side layers to the strip. The vortices occurring from the side walls become stronger than the initial vortices that arose from the strips. At this time the maximum transverse velocity w changes rapidly from 0.4 to 1.3. Later, the whole domain is strongly unstable and the resolution of the simulation

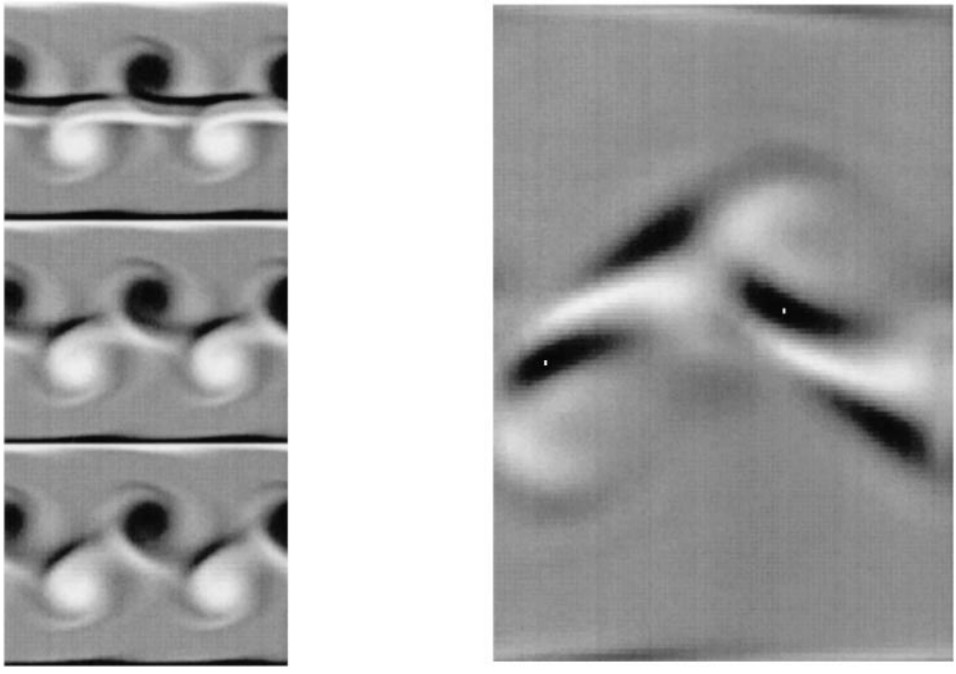

FIG. 11. Departure from the two-dimensional nature of magnetohydrodynamics duct flows. Left: view over two wavelengths of the y-component of the vorticity in the planes ($y = -a, -a/2, 0$). Right: view over one wavelength only of the perturbation in the y-component of the velocity in the plane ($y = 0.5$).

becomes too weak. However, no numerical instability in the form of a sudden overflow appears, which shows that the numerical scheme is reliable.

5.4. *Unstable Flow in a Duct with All Walls Insulating*

Since the side layers become unstable soon after the shear layer between the strips, and a long time before its vortices reach the sides of the duct, another run under the same conditions but without the conducting strips is performed to find out how unstable the flow would be without any special device. Therefore a fully insulating duct is considered here. Since there are no experimental data in that case, the wavelength of the previous simulation is chosen as a first attempt to model this flow. The Reynolds number is again based on the mean velocity, based on the constant flow rate. The initial perturbation is the similar to the previous one, now located in the boundary layers attached to the side walls.

The perturbation needs a much longer time than in the previous section, in order to be amplified (Fig. 12). There is now almost no three-dimensional effect in the components of velocity perpendicular to the magnetic field since no electrical discontinuity happens to be

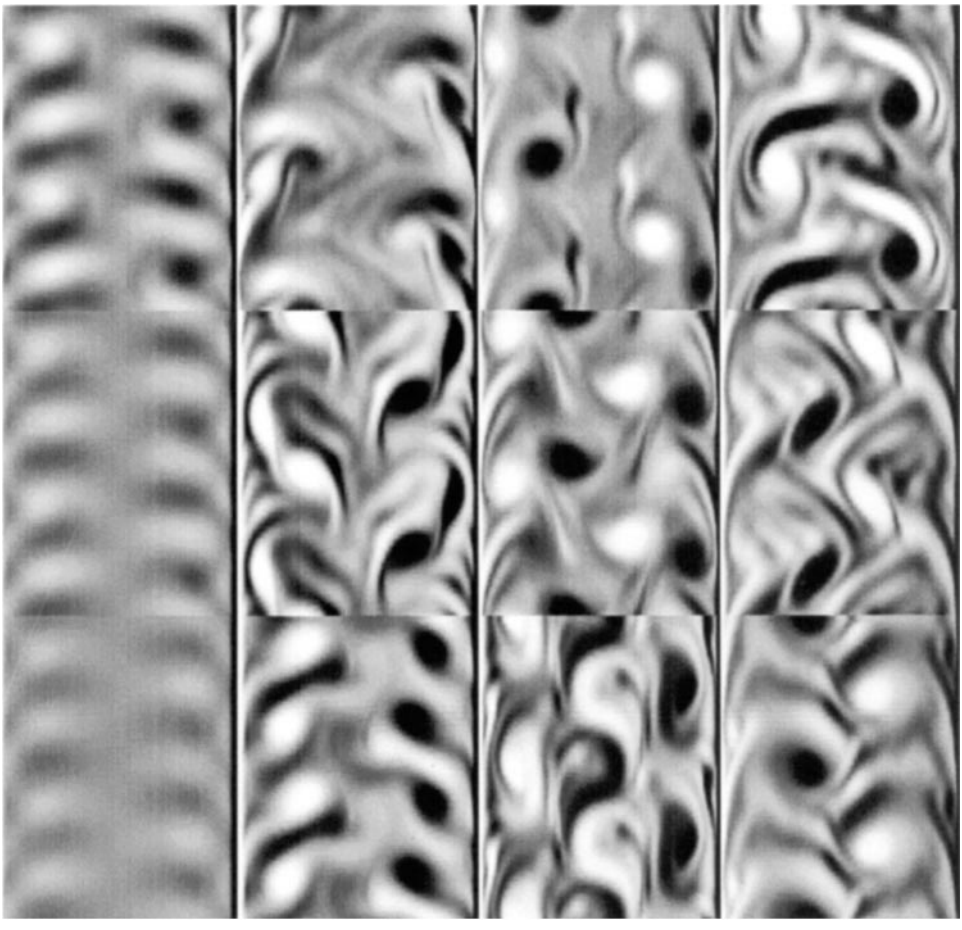

FIG. 12. Evolution of the unstable magnetohydrodynamic boundary layers at the walls parallel to the magnetic field in an electrically insulated duct. View of the y-component of the vorticity in the plane ($y = 0$). The frames are ordered from bottom to top and from left to right at the dimensionless time intervals 52.5, 55.0, 57.0, 60, 62.5, 65.0, 67.5, 70.0, 72.5, 75.0, 77.5, and 80.0 from the initial perturbation.

at the Hartmann walls as in the case of the conducting strips. When some vortices appear, they are located close to the side walls and extend to the bulk of the flow, although they do not reach the central core of the flow. The wavelength of the perturbation is half the length of the computation domain in the axial direction, until the vortices coming from a side wall meet the vortices coming from the opposite side wall. At this stage, the vortices coalesce to form a larger structure with a wavelength equal to the length of the domain. After 70 dimensionless units of time, the instability has not reached such a stage that the resolution of the grid becomes as poor as in the run with the conducting strips.

6. CONCLUSION

A stable and consistent scheme for finite volume computation of MHD flows at negligible magnetic Reynolds number has been presented and tested on unsteady duct flows. Analytical boundary conditions for the velocity and the currents at the walls perpendicular to the magnetic field were combined with the numerical boundary conditions for electrically conducting walls, allowing three-dimensional simulations at high Hartmann number. It is shown that such flows are unstable with or without turbulence promoters such as conducting strips. These turbulence promoters certainly increase the instability of duct flows, but the Reynolds numbers appropriate for fusion-reactor problems are much higher than in this paper. It is therefore expected that no device is needed to create turbulence, at least for the conditions of the last simulation where a straight duct is electrically insulated on its whole interior surface.

ACKNOWLEDGMENTS

The author is thankful for the support of Professor U. Müller, for the advice of L. Bühler about the physics of MHD flows, and for the help of C. Günther in numerical analysis. L. Lenhart has introduced the author to his code and to the code of A. Sterl, which were the starting points for the development of the code described in this paper. The fast Poisson solver using Fourier transform and written by T. Flassak at the University of Karlsruhe was used to solve the pressure equation. R. Mößner has dealt with the various aspects of the main frame computer's operating system, and the author is grateful to the people of the Forschungszentrum Karlsruhe.

REFERENCES

1. A. Sterl, Numerical Simulation of liquid–metal MHD flows in rectangular ducts, *J. Fluid Mech.* **216**, 161 (1990).
2. L. Lenhart, *Magnetohydrodynamik in Rechteckgeometrien, Volle numerische Simulation*, FZKA-report No. 5317, Forschungszentrum für Technik und Umwelt, Karlsruhe (1994).
3. A. L. Ting, J. S. Walker, T. J. Moon, C. B. Reed, and B. F. Picologlou, Linear-stability analysis for high-velocity boundary layers in liquid–metal magnetohydrodynamic flows, *Int. J. Engrg. Sci.* **29**, 939 (1991).
4. J. S. Walker, Magnetohydrodynamic flow in rectangular ducts with thin conducting walls, *J. Mécanique* **20**, 79 (1981).
5. L. Bühler, *Magnetohydrodynamische Strömungen flüssiger Metalle* in *allgemeinen dreidimensionalen Geometrien unter der Einwirkung starker, local variabler Magnetfelder*, FZKA-report No. 5095, Forschungszentrum für Technik und Umwelt, Karlsruhe (1993).
6. J. C. R. Hunt, Magnetohydrodynamic flow in rectangular ducts, *J. Fluid Mech.* **21**, 577 (1965).
7. J. Kim and P. Moin, Application of the fractional step method to incompressible Navier–Stokes equations, *J. Comput. Phys.* **59**, 308 (1985).
8. J. Blair Perot, An analysis of the fractional step method, *J. Comput. Phys.* **108**, 51 (1993).

9. C. Günther, Conservative versions of the locally exact consistent upwind scheme of second order, *Int. J. Numer. Methods in Engrg.* **34**, 793 (1992).
10. Ch. Hirsh, *Numerical Computation of Internal and External Flows* (Wiley, New York, 1990), Vol. 2, p. 525.
11. Y. Shimomura, Large eddy simulation of magnetohydrodynamic turbulent channel flows under a uniform magnetic field, *Phys. Fluids A* **3**, 3098 (1991).
12. L. Leboucher, Numerical simulation of two-dimensional unsteady MHD duct flows, in *Proceedings of the Eigth Beer-Sheva International Seminar on* MHD *Flows and Turbulence, 25–29 Feb. 1996, Jerusalem, Israel*.
13. Y. B. Kolesnikov, Two-dimensional turbulent flow in a channel with inhomogeneous electrical conductivity of the wall, *Magnetohydrodynamics* **8**, 70 (1972).
14. L. Bühler, Instabilities in quasi-2-dimensional magnetohydrodynamic flows, *J. Fluid Mech.* **326**, 125 (1996).
15. F. Debray, *Measurement of the Onset of* MHD*-Turbulence Caused by a Step in the Electrical Conductivity in the Channel Walls of GALINKA II and Comparisons with Theoretical Models*, FZKA-report No. 5723 (1997).